COMET 2024 Student Internship Report

Rochelle Pun

Supervisors: Dr Milan Lazecky, Dr John Elliott

October 22, 2024

Abstract

This project explores crustal deformation and active tectonics in the Hindu Kush and central Afghanistan through advanced InSAR processing techniques and analytical modeling. In this project, we processed initial ascending and descending line-of-sight frames from Sentinel-1 interferograms using novel techniques such as reunwrapping, ionospheric and solid earth tides corrections. After decomposing the frames into east-west and up-down velocities, we identified a suitable study region and applied a similar methodology to process and manually merge additional frames along the Herat fault. Finally, we used Bayesian inversion to test our velocity profiles against a synthetic screw dislocation model. Our analysis estimates the right-lateral slip rate along the Herat fault to be around 1.5-2 mm/yr, with an upper limit of 5 mm/yr. This aligns with Quaternary slip rates reported in the literature and offers valuable insights into assessing the seismic hazard in the region.

Plain Language Summary

Afghanistan is prone to large, devastating earthquakes due to its location within a major tectonic collision zone. However, due to limited accessibility and a lack of GPS stations, research into the region's active tectonics has been restricted. Throughout this project, we processed satellite data to remotely image surface deformation in central Afghanistan. Using analytical modelling, we then constrained key information about the seismic activity of the Herat fault. While further research is necessary to fully understand the dynamics at play, this work provides valuable insights into assessing the seismic hazard of the region, particularly for the cities of Herat and Kabul.

Contents

1 Introduction

The Hindu Kush region presents a unique opportunity to study a diverse range of active tectonic processes, from the terminal stage of slab subduction (*Kufner et al.* (2017)) to continental deformation associated with the Alpine-Himalayan orogeny. It is a region characterized by active crustal deformation and faulting, with a long history of devastating earthquakes often occurring near major population centers, as demonstrated by the 2023 Herat earthquake (*Ambraseys and Bilham* (2003)). Despite its high seismic hazard, the area remains under-researched due to limited field accessibility and lack of global navigation satellite systems coverage. As a result, there are few reliable estimates of strain and slip rates, which are critical for understanding the tectonic behavior of the region and assessing seismic risk.

The aim of this project is to advance our understanding of crustal deformation and continental tectonics of the Hindu Kush region through the use of satellite radar interferometry. By determining how strain and deformation is accommodated in the region, this study contributes to a broader understanding of the tectonic processes within the India-Eurasia collision zone. These insights will also help inform assessments of seismic hazard distribution, particularly the risks posed to major population centers such as Kabul and Herat, which are located near active faults like the Chaman and Herat faults.

Nomenclature	
SAR	Synthetic Aperture Radar
InSAR	satellite SAR interferometry
COMET	UK's Centre for the Observation and Modelling of Earthquakes, Volcanoes and Tectonics
LiCSAR	Looking Into Continents from spaceborne SAR
LiCSBAS	LiCSAR method for Small Baselines
LOS	Line Of Sight
GACOS	Generic Atmospheric Correction Online Service for InSAR
SB	Small Baselines
NSBAS	New Small Baseline Subset
GNSS	Global Navigation Satellite Systems
GMT	Generic Mapping Tools
PyGMT	Python interface for the Generic Mapping Tools

1.1 Tectonic Setting

The present day tectonic setting in the Hindu Kush and surrounding areas, as shown in Figure 1 reveals crustal deformation resulting from the collision between the Indian subcontinent and Eurasia, with the Indian plate moving northward at a rate of approximately 4cm/yr relative to Eurasia (*Ischuk et al.* (2013)). Located at the western end of the Alpine-Himalayan orogenic belt, this region hosts a diverse range of active tectonic processes, reflecting the intense tectonic stress its subjected to. To the northeast, the Hindu Kush and Pamir mountains present a rare example of ongoing slab break-up, as the Indian plate subducts northward beneath Eurasia (as shown from the slab contours in Figure 1, after *Kufner et al.* (2017)). This process forces up the western Himalayas and causes the uplift of the Pamir Plateau, which is currently collapsing westward. This gravitational collapse, along with a portion of the north-south compression, is accommodated by westward material extrusion between major strike-slip faults, specifically the left-lateral Chaman fault and the right-lateral Herat fault. More recently, vertically partitioned fold-and-thrust deformation in the Tajik Depression is also thought to play a similar role in strain accommodation (*McNab et al.* (2019)). In northeastern Afghanistan, the Darvaz Fault and Vakhsh Thrust are among the most seismically active regions on the planet, with diffuse north-south trending ruptures extending southwards throughout central Pamir (*Elliott et al.* (2020)). While central Afghanistan is thought to be less seismically active, accreted blocks terranes throughout the region are separated by suture and fault zones, many of which are active and potential sources of seismic hazard (*Shroder et al.* (2022)).
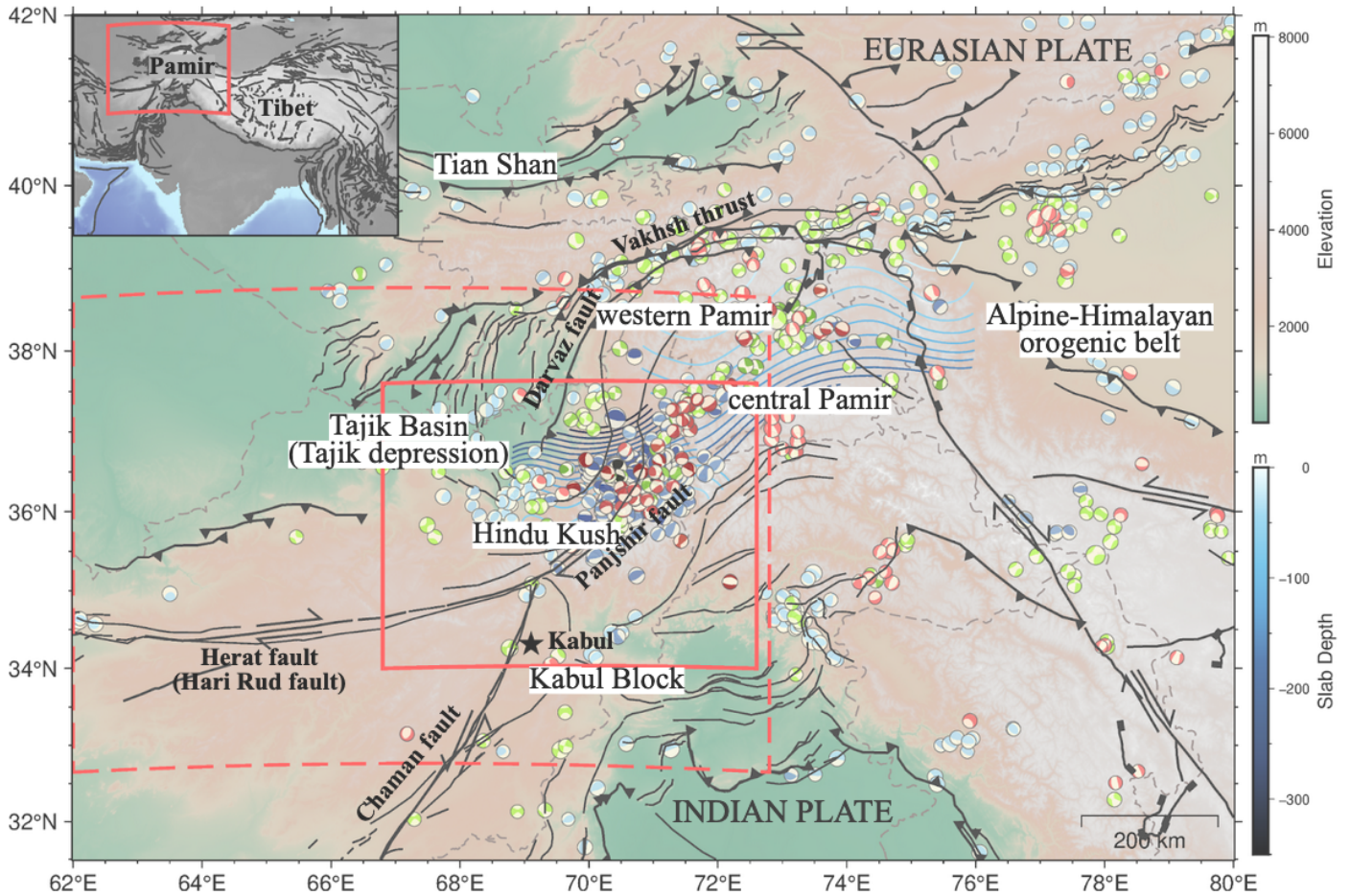
Figure 1: Tectonic setting of the Hindu Kush and the surrounding area. Major tectonic blocks and faults are marked by black lines (after *Styron et al.* (2010), *Taylor and Yin* (2009) and *Styron and Pagani* (2020)). The solid red line outlines the region shown in Figure 2, while the dotted red line indicates the study area covered in Figures 8, 9 & 10. Slab contours of the Hindu Kush (west) and Pamir zone (east) are from the slab model of *Hayes et al.* (2018), with seismicity data sourced from the Harvard CMT catalogue (Section B.2).

2 Methodology

2.1 Initial InSAR Frame Selection and Processing with LiCSBAS

We use Sentinel-1 unwrapped and geocoded interferograms automatically processed by LiCSAR and publicly available on the COMET–LiCSAR web portal (*Lazecký et al.* (2020)). Figure 2 shows ascending and descending frames that we have initially selected. Each frame covers approximately 250x250km at 0.001° (approximately 100m) resolution. Our original aim was to cover the Hindu Kush region in a manner similar to *Metzger et al.* (2021), expanding upon their work by applying novel processing techniques. Additionally, we wanted to resolve major faults within the Hindu Kush and Pamir mountains, particularly the diffuse north-south trending ruptures in central Pamir (*Elliott et al.* (2020)).

After a quick overview of the study area, we began with processing ascending frame 071A_05440_131313 and descending frame 078D_05435_131313 (see Figure 2). We believed that covering the triple junction between the Herat fault, the Chaman fault and the Panjshir fault would offer us unparalleled flexibility in the direction of which we could take our study further. Moreover, the varying topography and diverse land use covered by our initial frame pair serves as a good test for the limits of the LiCSBAS processing system.
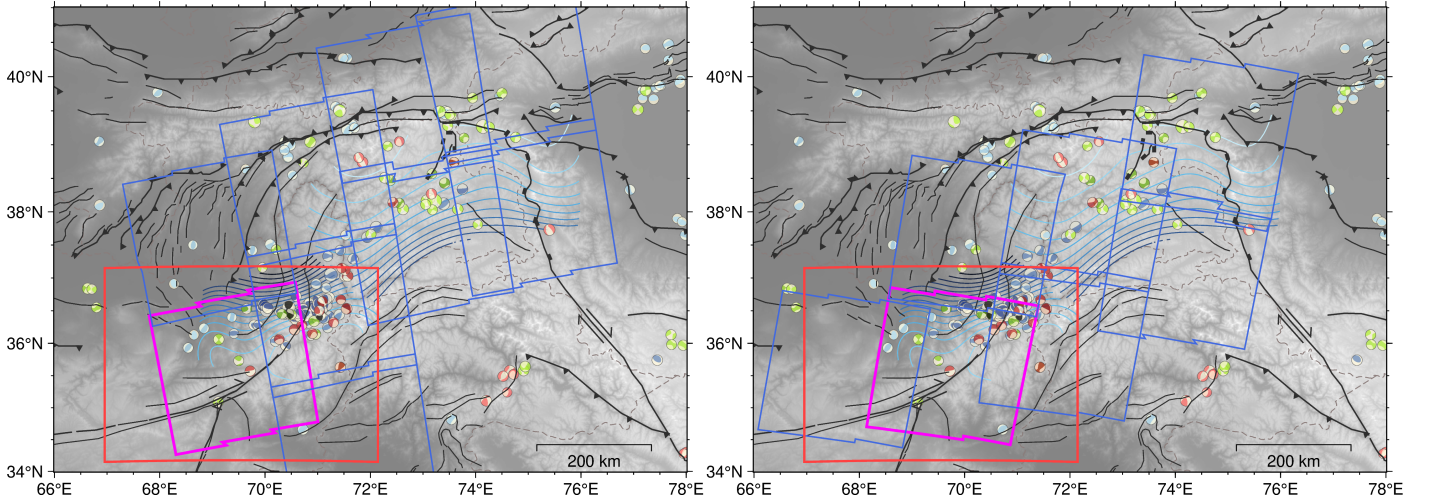
Figure 2: Ascending (left) and descending (right) frames originally selected to best cover the Hindu Kush region. Initial ascending frame 071A_05440_131313 and descending frame 078D_05435_131313 are shown in magenta. Area enclosed in red marks the zoomed-in region for Figures 3, 4, 6 & 7. Seismicity is limited to the network duration of the dataset. Note the particularly mountainous topography over the Hindu Kush which later proved to be challenging to image with InSAR.

The selected frames, spanning over an observation period from March 2016 to July 2024 were processed using COMET-LiCSBAS, an open-source package that processes LiCSAR-generated products for InSAR time series analysis[1] (*Morishita et al.* (2020)). The LiCSBAS processing flow involves five steps for data preparation (Steps 0–1 to 0–5) and six steps for time series analysis (Steps 1–1 to 1–6). We carefully selected processing parameters that were best suited to the challenging topography of the Hindu Kush region, often experimenting with novel processing techniques. Below, we briefly summarize and justify the key decisions made regarding these parameters. Further details (including a full list of parameters used in this study) can be found in Appendix B.1.

The unwrapped data was first down-sampled with a multi-looking factor of 10 at Step 0-2, resulting in a spatial resolution of approximately 1km. We then applied tropospheric noise correction using GACOS at Step 0-3, correcting for the effects of troposphere turbulence and stratification. Steps 0-4 and 0-5 were omitted throughout this study as we found it unnecessary to mask and clip our dataset. At Step 1-2, the original implementation of LiCSBAS identifies wrongly unwrapped interferograms by a loop closure check and drops them from further processing should they exceed a threshold. Here, we use a new nullification functionality as described by *Lazeckỳ et al.* (2024) that nullifies individual pixels with loop closure errors as opposed to dropping entire interferograms. This allows us to preserve good data regions where whole interferograms would otherwise be dropped due to potentially small unwrapping errors, an issue particularly relevant for mountainous areas. At Step 1-3, we used NSBAS Weighted Least Squares (WLS) function to derive mean displacement velocities from cumulative displacements instead of the conventional (unweighted) least-squares option. This is a subtle improvement that takes into account variance in coherence between pixels prior to the inversion. Lastly, at Step 1-6, we subtracted topography-correlated components linearly prior to spatio-temporal filtering. Although most of such height-correlated signals should have been reduced by GACOS, it is still a substantial source of noise in mountainous regions. Moreover, tectonic signals tend to be of longer spatial wavelength compared to variations in topography, making them less vulnerable to height-correlated filtering. For such reasons we believe that the signal-to-noise ratio improvement from this far out-weights the possibility of us accidentally removing signals of interest.

---

[1]We used an active development version of LiCSBAS available at github.com/comet-licsar/licsbas as 'dev' branch from the v1.2 release.

2.1.1 Reunwrapping

To further improve the quality of unwrapped interferograms that are inputted into the time series inversion, we implemented a full reunwrapping of the original wrapped interferograms with the use of the COMET licsar_extra repository (as described by *Lazeckỳ et al.* (2022), available at github.com/comet-licsar/licsar_extra). This approach first models and removes sources of phase delays from the original wrapped interferograms. This includes correcting for spatial phase ramps due to long wavelength signals (such as Solid Earth Tides), reducing height-correlated phase signals by correlation with an external digital elevation model, and removing tropospheric gradients with GACOS. After the unwrapping itself, the modeled sources of phase delays are added back to the final output. By reducing high phase gradients that are responsible for decorrelation and zonal unwrapping errors, we improve reliability of phase unwrapping and increase coverage of unwrapped pixels.
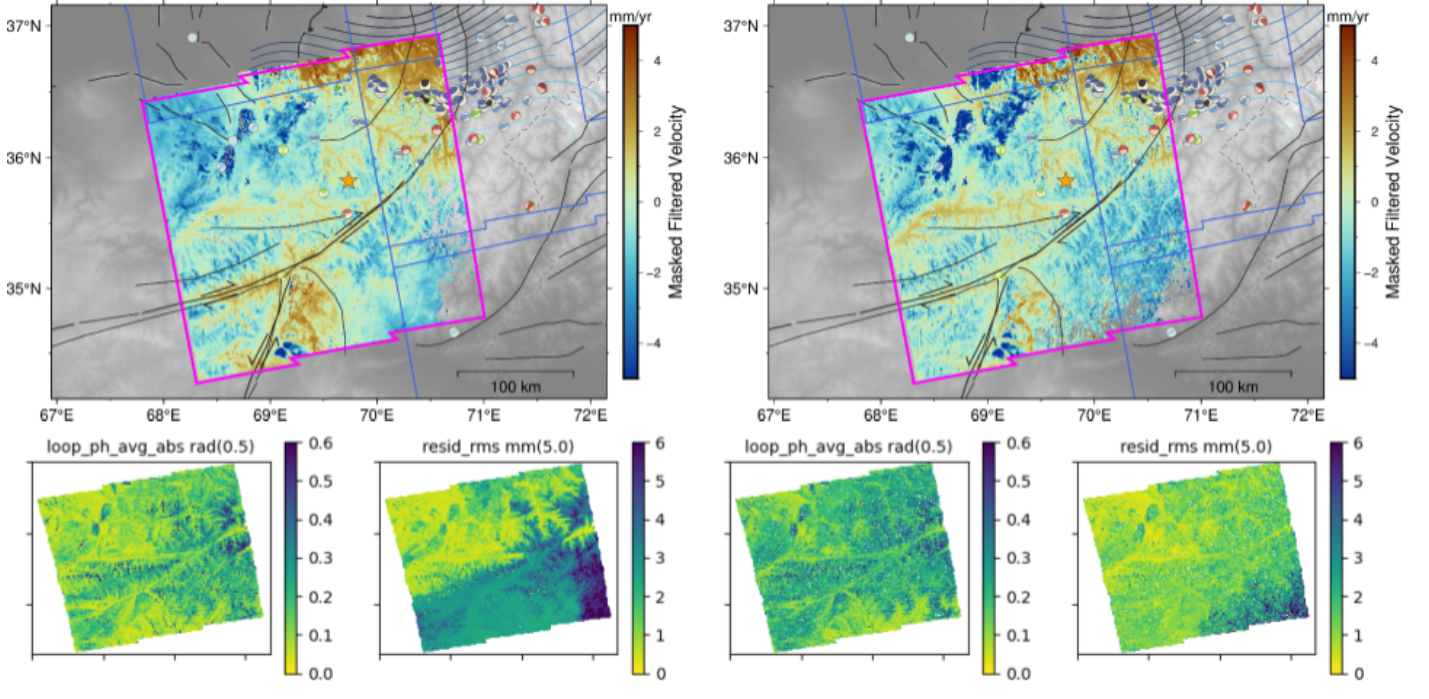

Figure 3: LiCSBAS Step 1-6 LOS velocity output (masked) for ascending frame 071A_05440_131313, without (left) and with reunwrapping (right), with the same masking parameters and linearly adjusted for the same SB inversion reference area (as indicated by the orange star). Average loop phase closure error (loop_ph_avg_abs rad) and inversion residual RMS error (resid_rms mm) for each output are shown below their respective frames.

Figure 3 demonstrates the impact of reunwrapping on the ascending frame 071A_05440_131313. The inversion residual Root-Mean-Square (RMS) error are higher for pixels with more unwrapping errors and serves as an indicator of unwrapping quality. By comparing the residual RMS errors between the two inversions, we can see that reunwrapping significantly improves the quality of unwrapping, particularly in mountainous regions in the southern end of the frame.

2.1.2 Initial Ascending and Descending LOS Velocity

When we applied the same processing parameters to the descending frame, we quickly realized that its quality was significantly lower than that of the ascending frame. To address this, we increased the RMS loop phase threshold by tenfold at Step 1-2, which improved the availability of interferograms in the network. We also manually specified a stable reference point and applied generous masking parameters. Despite these efforts, a substantial portion of the frame— particularly the mountainous regions to the east— suffered from severe interferometric decorrelation, which we had to mask.
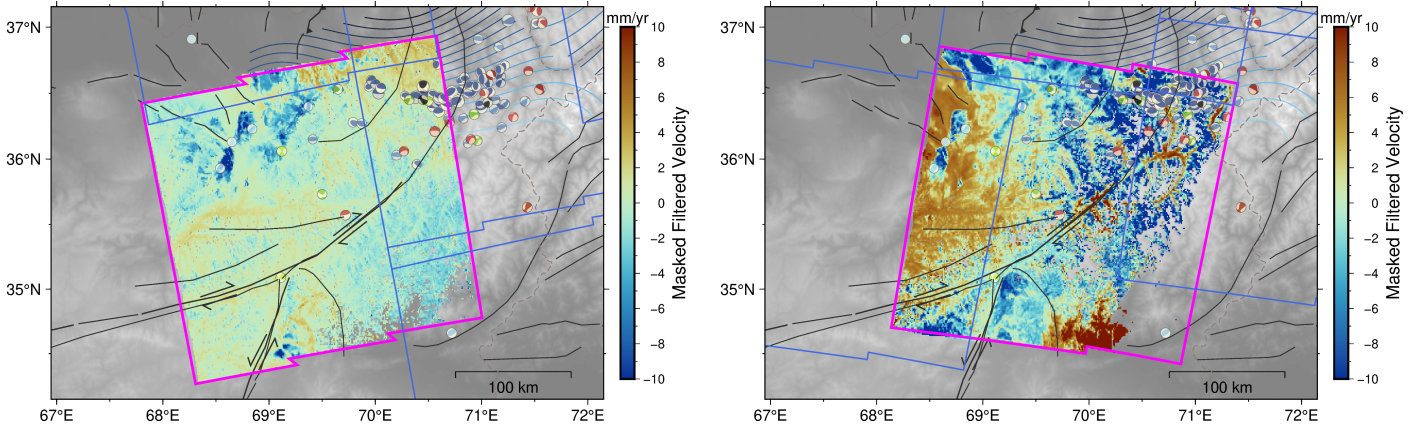
Figure 4: LiCSBAS Step 1-6 LOS velocity output for ascending frame 071A_05440_131313 (left) and descending frame 078D_05435_131313 (right), with masking and bilinear 1D deramping applied (see Section 2.1.3 for justification on bilinear 1D deramping). Note the significantly lower data quality for the descending frame, which we interpret as evidence of interferometric decorrelation caused by surface glaciers.

2.1.3 Ionosphere and Solid Earth Tides (SET) correction

Time series analysis of our initial velocity outputs (Figure 5) revealed a sinusoidal signature present throughout the dataset. As this was a regularly repeating signal, we theorized that it could be caused by long-wavelength sources, such as seasonal fluctuations due to ionospheric influence and SET. To resolve this, we applied ionospheric and SET correction models derived from the S1-ETAD product (*Gisinger et al.* (2022)) to estimate and remove interferometric phase contributions from modelled sources that could otherwise be misinterpreted as tectonic signals.
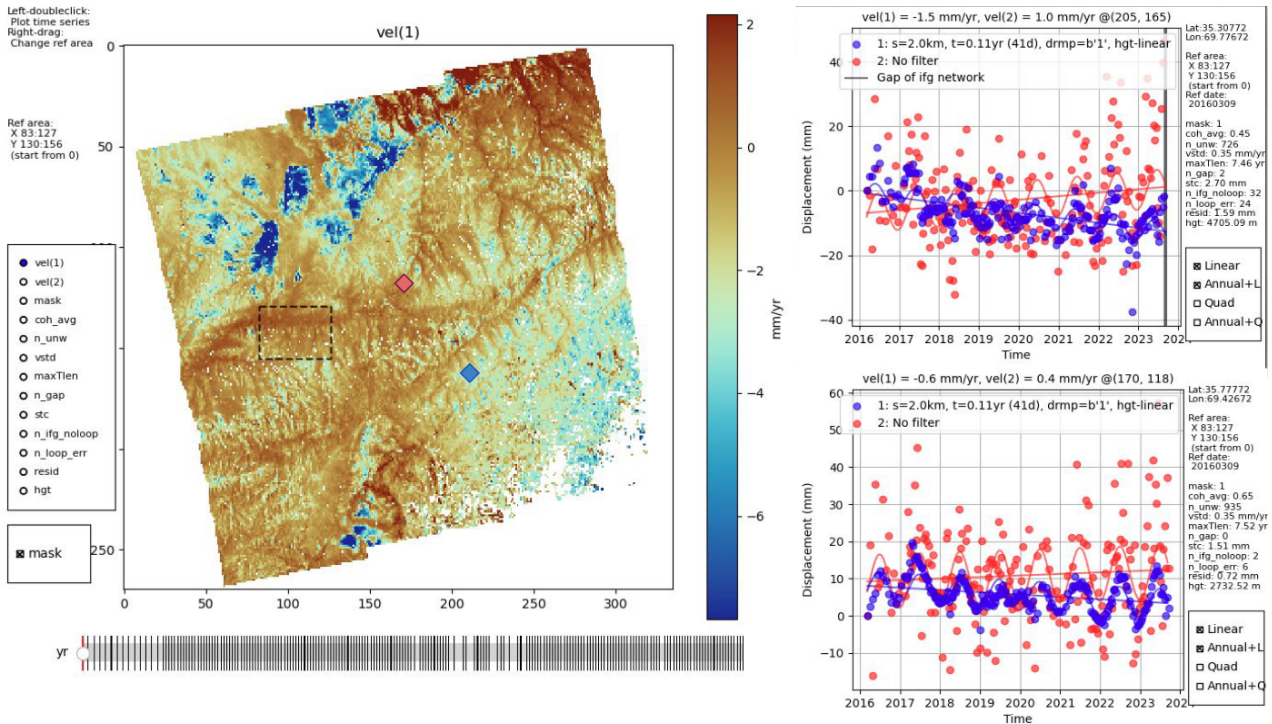

Figure 5: LiCSBAS Step 1-6 LOS velocity output (masked, with deramping) for ascending frame 071A_05440_131313, with time series analysis for the red-diamond-indicated pixel and the blue-diamond-indicated pixel at the top and bottom right respectively. Reference area for both time series is indicated by the region selected in black rectangle. Blue and red data points represent displacement values with and without the application of LiCSBAS Step 1-6 spatio-temporal filtering, height-correlated signal subtraction, and bilinear 1D deramping. Note the sinusoidal signal present in all time series plots, which we attribute to the influence of ionosphere and SET.
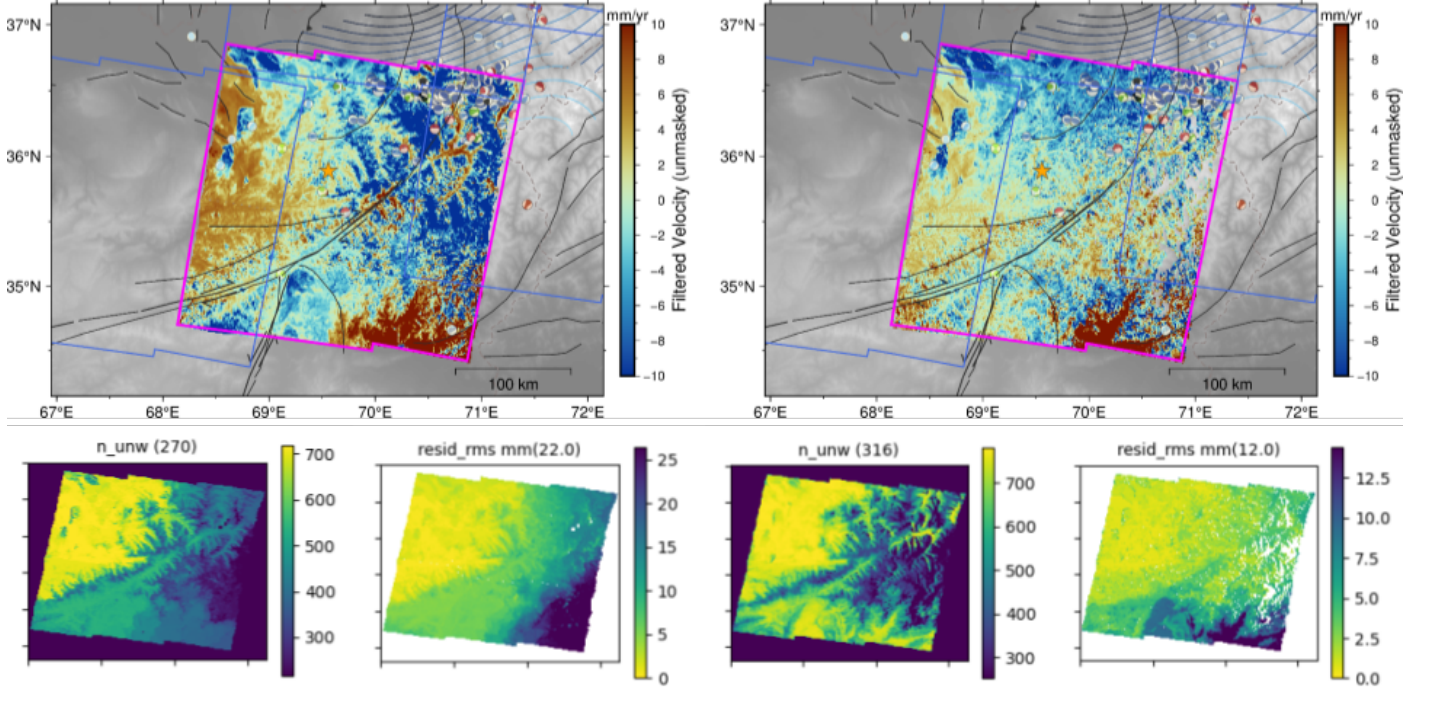
Figure 6: LiCSBAS Step 1-6 LOS velocity output (unmasked) for descending frame 078D_05435_131313, without (left) and with ionosphere and SET correction (right), linearly adjusted for the same SB inversion reference area (indicated by the orange star). Number of unwrapped interferograms (n_unw) and inversion residual RMS error (resid_rms mm) for each output are shown below their respective frames.

Figure 6 illustrates the impact of ionosphere and SET correction on the descending frame 078D_05435_131313, applied prior to unwrapping. From the lower residual RMS error on the corrected inversion, we can see that ionosphere and SET correction reduces unwrapping errors and unwraps more pixels. As ionosphere and SET correction is a computationally expensive and demanding procedure, we have decided to replace this with deramping at LiCSBAS Step 1-6. While we were initially concerned that this might remove some of the regional tectonic signal, the fact that the correction eliminated ramp-like features in both the number of unwrapped interferograms and the residual RMS error suggests that most of the ramping is due to ionospheric and SET effects, rather than regional tectonic influences. Therefore, moving forward, we applied a bilinear 1D deramping in addition to the usual filtering at LiCSBAS Step 1-6.

2.1.4 Single-frame Decomposition

With at least two independent measurements from ascending and descending orbits, we can then decompose our LOS velocities into north-south (V_N), East-West (EW, V_E) and vertical (UD, V_U) velocities. This is done by solving a linear system of equations between our LOS velocities (V_{asc} and V_{desc}) and our component velocities:

$$\begin{bmatrix} V_{asc} \\ V_{desc} \end{bmatrix} = \begin{bmatrix} sin(\theta_{asc})cos(\alpha_{asc}) & sin(\theta_{asc})sin(\alpha_{asc}) & -cos(\theta_{asc}) \\ sin(\theta_{desc})cos(\alpha_{desc}) & sin(\theta_{desc})sin(\alpha_{desc}) & -cos(\theta_{desc}) \end{bmatrix} \begin{bmatrix} V_E \\ V_N \\ V_U \end{bmatrix} \quad (1)$$

where θ_{asc} and θ_{desc} denote the radar incidence angle, and α_{asc} and α_{desc} denote the azimuth of the along-track satellite heading, for a matching pair of ascending and descending frames respectively. Both θ and α vary pixel-by-pixel.

Equation 2 presents an undetermined system with three unknowns and only two input datasets. To solve this linear system of equations analytically, we hereby assume that north-south velocity $V_N = 0$ for our predominantly east-west orientated fault.

$$\begin{bmatrix} V_{asc} \\ V_{desc} \end{bmatrix} = \begin{bmatrix} sin(\theta_{asc})cos(\alpha_{asc}) & -cos(\theta_{asc}) \\ sin(\theta_{desc})cos(\alpha_{desc}) & -cos(\theta_{desc}) \end{bmatrix} \begin{bmatrix} V_E \\ V_U \end{bmatrix} \tag{2}$$

Although we know that the collision of the Indian plate with the Eurasian plate - the driving force behind the Himalayas - is predominantly north-south orientated, we reason that most of the north-south motion is accommodated by rapid slip along the Chaman fault and fold-and-thrust deformation in the Tajik depression[2]. Combined with the fact that LOS measurements are least sensitive to displacements in the north-south direction due to the near polar orbits of Sentinel-1, we believe this assumption is a reasonable approximation of reality provided that our fault of interest remains oriented in an east-west direction.
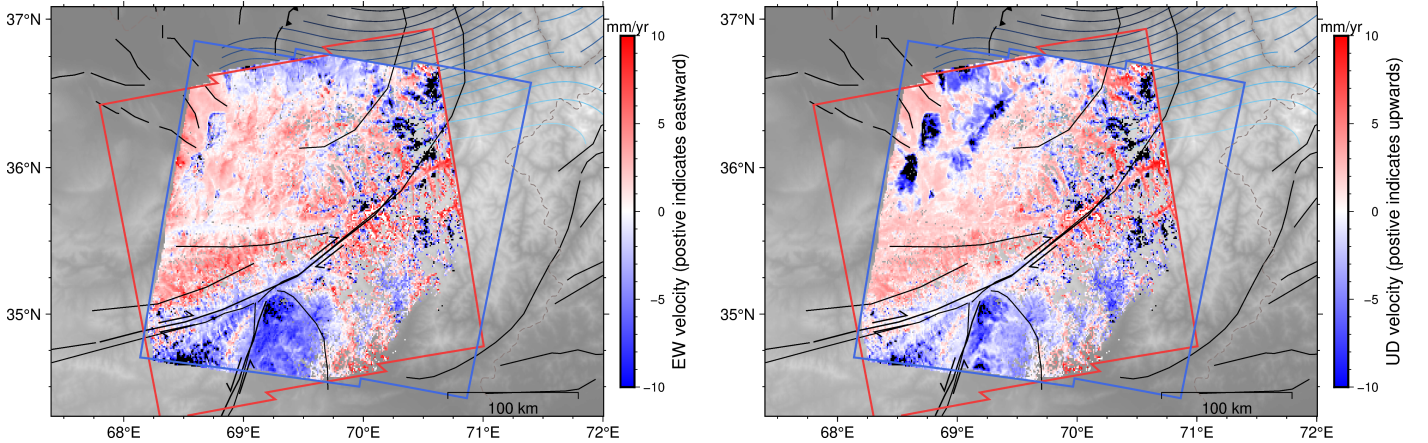

Figure 7: LiCSBAS-decomposed EW (left) and UD (right) velocities for ascending frame 071A_05440_131313 (red) and descending frame 078D_05435_131313 (blue). Positive values (red) indicates eastward and upward displacement respectively.

LOS velocity decomposition was performed using LiCSBAS (*Morishita et al.* (2020)). When multiple frames were involved, decomposition was carried out on a frame-by-frame basis prior to frame merging.

2.2 Final Frame Selection and Processing

Based on our experience processing the initial descending frame (and later from inspecting the average coherence of the study area (Figure 19)), we realized that the Hindu Kush mountains in the east, which dominated the initial study area, suffered from severe interferometric decorrelation. Most of this had to be masked and would therefore not be ideal for further study. Moreover, as *Metzger et al.* (2021) had already conducted a detailed study of the Tajik basin to the north-west, we opted to avoid that region to prevent overlap. This left us with the choice between the Chaman fault to the south and the Herat fault to the west. While the Chaman fault has been relatively well studied in the literature, we realized that there are no existing modern slip rate estimates despite the devastating series of earthquakes that occurred in 2023. This, along with the high-quality interferograms in the west (Figure 7), convinced us to shift our study area to focus on the Herat fault, a 730-km-long, right-lateral fault that runs laterally across Afghanistan.

The lack of GNSS data in Afghanistan prevented us from using GNSS-interpolated north rates for decomposition and frame merging (*Watson* (2022)). To address this, we manually decomposed each frame and adjusted it by the difference between its median and that of the primary frame, assuming a linear velocity trend away from the initial ascending and descending frames. This was also applied to the noise indices, where the "decomposition" from LOS frames to their respective variables was done as shown in Appendix B.2.

---

[2]Although this is contested by the 2023 Herat earthquakes, which had a east-west striking fault plane solution indicating compression in the north-south direction. This is further discussed in Section 3.
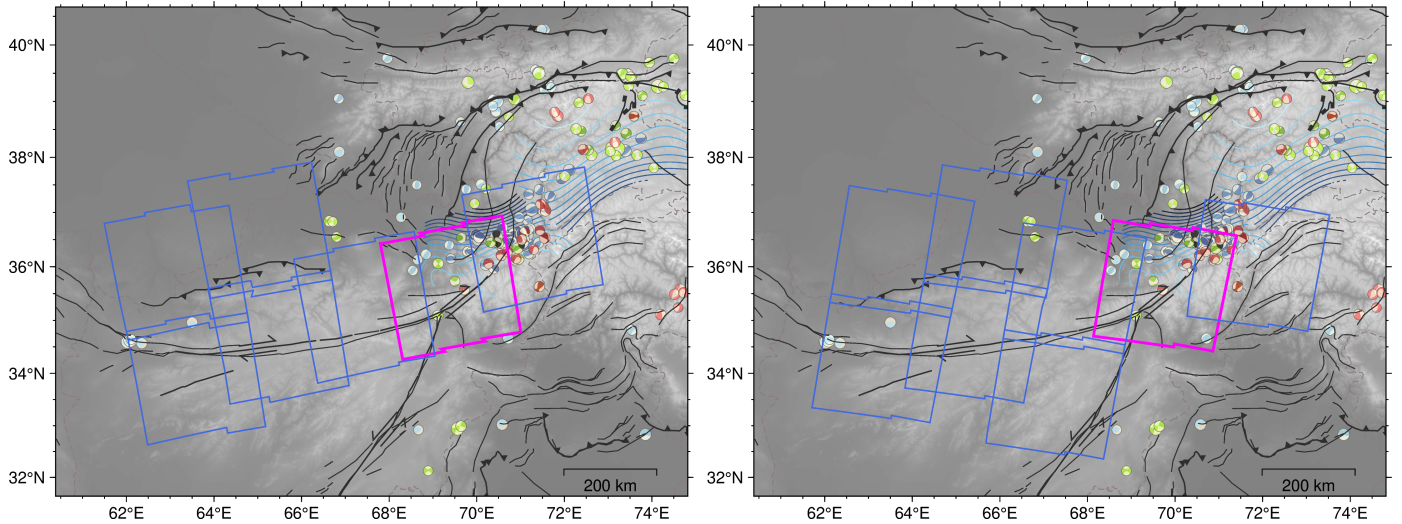
Figure 8: Final ascending (left) and descending (right) frames selected to best cover the Herat fault, intentionally omitting the 2023 Herat earthquakes to the west both spatially and temporally. Initial ascending frame 071A_05440_131313 and descending frame 078D_05435_131313 are shown in magenta, with a full list of frame IDs available in Appendix B.1.3.

2.3 Analytical Modelling of the Herat fault

Ground deformation through the interseismic period of an active fault can be modelled by considering steady slip on a screw dislocation model:

$$v(x) = \frac{s}{\pi} \tan^{-1}\left(\frac{x}{d}\right) + c \tag{3}$$

Where v, the fault-parallel surface velocity is a function of the perpendicular distance from the fault, x, the right-lateral slip rate, s and the locking depth, d on a vertical fault. c is the arbitrary offset constant. A typical interseismic signal should thus approximate the shape of an arctan function, where ground displacement decreases from the far-field to zero at the fault plane (*Savage and Burford* (1973)). By constraining the right-lateral slip rate and locking depth of the Herat fault, we can assess its seismic potential and the distribution of strain within the crust, both of which are crucial for evaluating the seismic hazard in the region.

Equation 3 requires fault-parallel velocities, which given the predominantly E-W orientation of the Herat fault, we approximate with E-W velocity. We acknowledge that true fault-parallel velocities would yield a stronger along-fault signal, and this remains an area for future improvement.

2.3.1 Analytical Modelling of Selected Profiles

In order to compare ground deformation across the Herat fault with the screw dislocation model, we must first acquire fault-perpendicular velocity profiles. We began by modifying the interseismic practical provided by Andrew Watson (*Watson* (2021)) to directly apply on our final decomposed and merged EW velocity dataset (Figure 9). The original version of the code takes in LiCSBAS-processed frames as inputs and directly decomposes ascending and descending LOS velocities into fault-parallel and vertical velocities. However, some of the frame boundaries in our study area cut across the Herat fault, with different sides of the fault imaged by different frames (as seen in Figure 8). To address this, we modified the code to take in our final merged frames as input, allowing us to extend our profile plots - and corresponding analytical models - across the entire study area. We then applied Bayesian inversion to profile plots at regular intervals of approximately 50 km along the fault, with each profile extending 40-60 km on either side of the fault and a bin width of 5 km. The best model for each profile is plotted, and the one with the highest sensitivity to the screw dislocation model (Figure 10) is identified as the upper limit for the right-lateral slip rate and locking depth of the Herat fault.
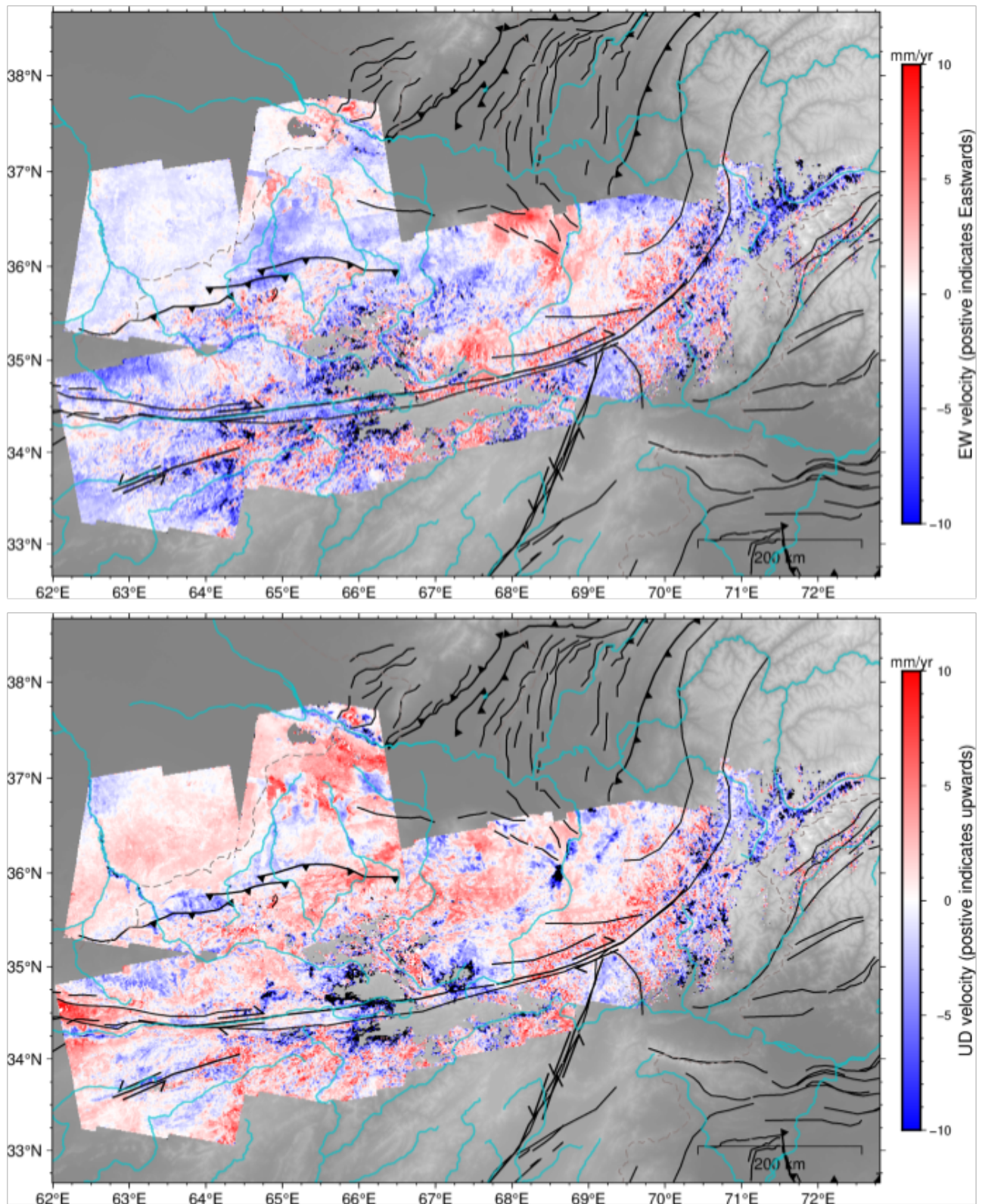
Figure 9: Final decomposed and merged EW (top) and UD (bottom) velocities for our study area, with frame coverage shown in Figure 8. A full list of decomposition pairs, processing and masking parameters can be found in Appendix B.1.3. Rivers and freshwater aquifers (cyan) are potential sources of subsidence.
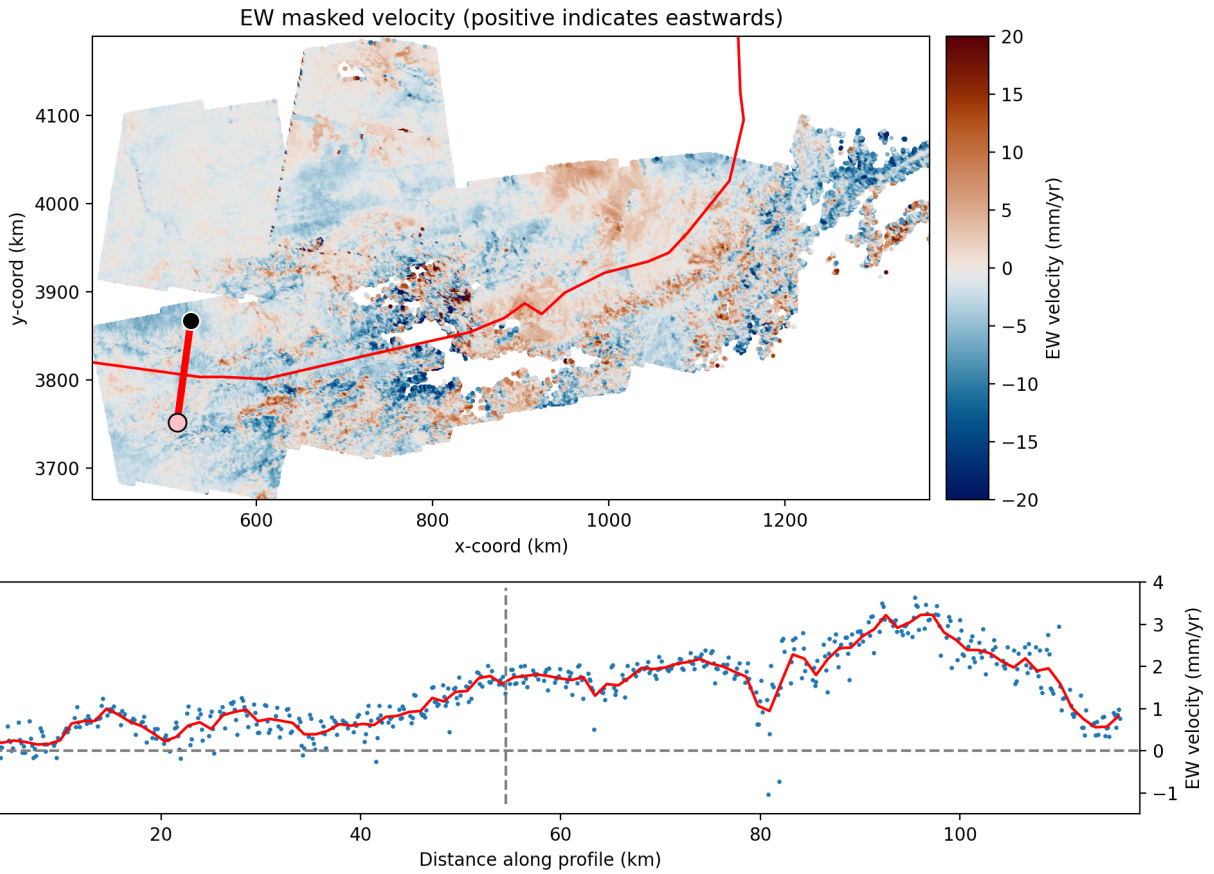
Figure 10: Profile plot of EW velocities (masked, normalized to xy coordiates in km (see Figure 9) across the Herat fault, identified as having the highest sensitivity to the screw dislocation model. The start and end points are marked by pink and black circles respectively, with the thin red line indicating the right-lateral Herat fault, visible in the cross-section as the vertical black dotted line.

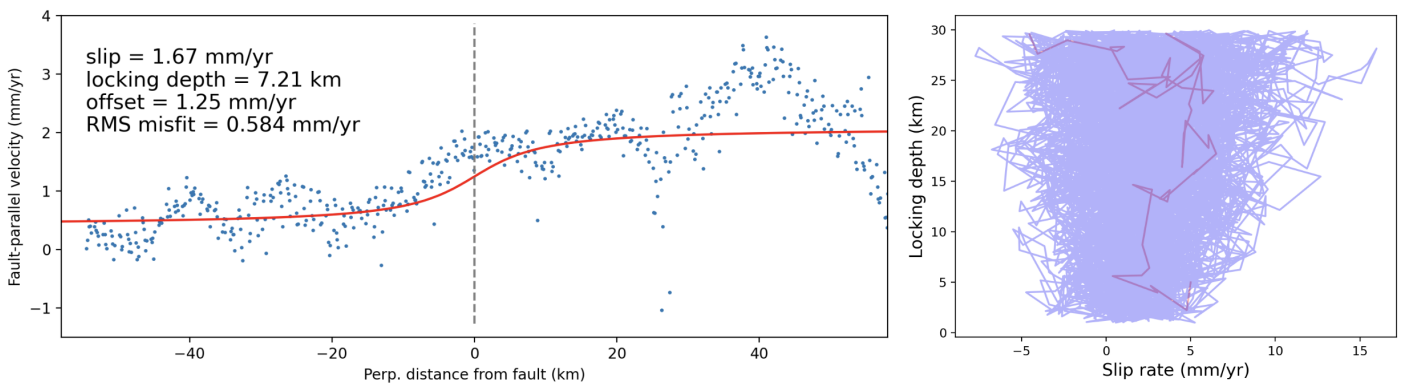# 3 Results and Discussion

Figure 11: Walker plot (right) and the best-fitting model (left, in red over the profile plot seen in Figure 10) for Bayesian inversion over 10,000 iterations. The first 100 iterations are highlighted in red in the Walker plot.

Figure 11 shows the best-fitting model from our Bayesian inversion, with a modelled slip rate of 1.67 mm/yr and a locking depth of 7.21 km. Interestingly, this model has a lower slip rate and locking depth than the mean of our inversions (Figure 12), which show a mean slip rate of 2.43 mm/yr and a locking depth of 17.24 km respectively. This suggests that while higher values may be more common,
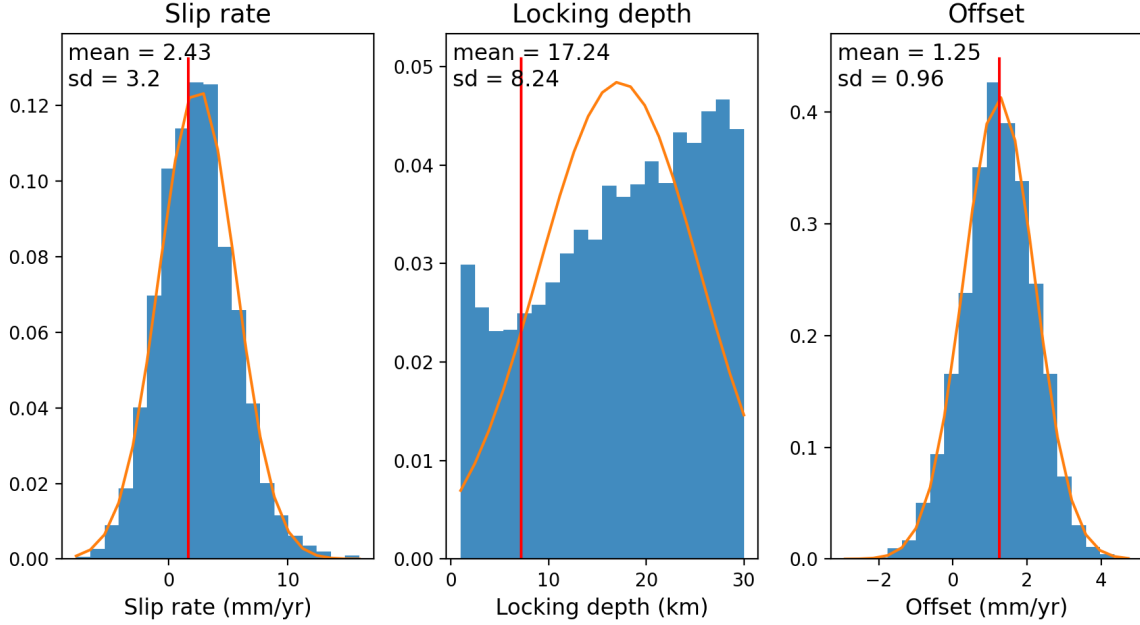
12

Figure 12: Histograms of slip rate, locking depth, and model offset for our Bayesian inversion models. The best-fitting model values (i.e. Figure 11) are indicated by vertical red lines.

they are likely biased by extreme values in the dataset and therefore do not fit the arctan function as well.

Herat Fault Characterization

Realistically, the right-lateral slip rate of the Herat fault is around 1.5-2 mm/yr, and we are confident that it does not exceed 5 mm/yr. We selected the profile with the highest sensitivity to the screw dislocation model, making 2 mm/yr the highest observable slip rate in our dataset. However, we observe that the slip rate is highest to the west of the fault, sometimes exceeding 3 mm/yr, and decreases to a negligible amount towards the east. This suggests that the observed slip could be approximately 1 mm/yr higher than estimated, though we unfortunately lack sufficient high-quality data to fully resolve the westernmost boundary of our dataset. A slip rate of 3 mm/yr would be more consistent with the long-term slip rates derived from geological stream channel offsets presented by *Sborshchikov et al.* (1981). In terms of locking depth, the Walker plot and histograms in Figures 11 & 12 indicate that it is poorly constrained, leading us to conclude that we cannot reliably determine it from our dataset. Lastly, we observe that the fault plane from our profile plots is often slightly north of the mapped fault line. Since this is likely a sign of stress accumulation rather than poor geological mapping, we infer that the Herat fault is likely north-dipping.

Bringing all of this together suggests that the Herat fault is a right-lateral strike-slip fault that dips slightly North and is locked in the West and creeping in the East. The surprisingly low slip rate can be explained by the fact that the Herat fault is not ideally oriented to accommodate stress from the Alpine-Himalayan orogeny, as well as strain from the western collapse of the Pamir mountains being accommodated by active north-south trending reverse faults in the Tajik Basin. From this, we infer that right-lateral strain buildup along the Herat fault is likely minimal, resulting in a long recurrence interval and a lower seismic hazard compared to more active faults in Afghanistan.

Complications from the 2023 Herat earthquakes

On October 7, 2023, four magnitude 5.5+ earthquakes struck the Herat province, with epicenters located slightly west of our study area. Inversion of seismic source parameters from InSAR displacements (*Liu et al.* (2024)) reveals blind northward thrust faulting with a minor component of right-lateral slip on an unmapped thrust fault located to the north of the Herat fault.

There are two possible explanations for this: either the earthquakes occurred on a blind thrust fault that is separate and independent from the Herat fault, or that the Herat fault itself may be depth-partitioned, exhibiting right-lateral motion at shallower depths and transitioning to north-dipping compressional behavior at greater depths beneath a detachment. The latter is plausible, especially as *McNab et al.* (2019) observed vertically partitioned deformation in the Tajik basin to the north. It is possible that the series of north-dipping thrust faults observed beneath the Tajik Basin extends southwards towards the Herat fault. Depth partitioning would also explain the short recurrence interval for large historic earthquakes along the Herat fault despite seismic hazard models concluding relatively lower seismic hazard near Herat (*Ambraseys and Bilham* (2003), e.g. *Boyd et al.* (2007)). Regardless of the underlying mechanism, the 2023 Herat earthquakes reveal the structural complexity of the Herat fault and highlight the limitations of both our study and the use of InSAR imaging as a method.

3.1   Sources of Errors and Limitations

The primary sources of error in InSAR processing stem from severe interferometric decorrelation, which are driven by the region's complex topography and frequent surface changes. We observe gaps present during the winter months throughout the dataset, which we attribute to snowfall. This, combined with the presence of freshwater aquifers within the Hari basin has contributed to poor phase unwrapping along the eastern end of the Herat fault (*Shroder et al.* (2022)). This undermines the strength and reliability of our deformation signal and significantly reduces the confidence in our velocity estimates. While the influence of atmospheric errors cannot be ignored, they are likely less significant compared to those arising from surface changes. To address this, future studies could look into the use of advanced deep learning techniques for extracting subtle deformation signals that are otherwise difficult to detect. Additionally, more advanced data smoothing methods could improve confidence in the dataset, particularly in low-coherence areas. With sufficient quality data, future studies could even look into high-resolution imaging to resolve the complex diffuse suture along the Herat fault.

The near polar orbits of Sentinel-1 meant that LOS measurements are least sensitive to displacements in the north-south direction. While this is not a significant issue for the east-west trending Herat fault, fault solutions for the 2023 Herat earthquakes, which indicate north-south compression, raise concerns about this limitation (*Liu et al.* (2024)). Improving the ability to image north-south displacements, through the use of bursts or data from future Earth observation satellite missions, will be crucial for capturing strain accumulation in the north-south direction. This, combined with a more robust GNSS network, will enable strain modelling and allow us to resolve structural complexities along the Herat fault.

4   Conclusion

The Hindu Kush region, and by extension Afghanistan, is a zone of intense tectonic activity driven by the collision between the Indian subcontinent and Eurasia. This project aims to constrain crustal deformation and active tectonics in the region through advanced InSAR processing techniques and analytical modelling. We began by processing initial ascending and descending LOS frames around Hindu Kush, employing novel techniques such as reunwrapping, ionospheric and SET corrections. After decomposing the frames into EW and UD velocities, we identified a suitable study region and applied a similar methodology to process and manually merge additional frames along the Herat fault. Finally, we applied Bayesian inversion to test our velocity profiles against a synthetic screw dislocation model. We estimate the right-lateral slip rate along the Herat fault to be approximately 1.5-2 mm/yr, with an upper limit of 5 mm/yr, consistent with Quaternary slip rates reported in literature. While further research is needed to fully understand the structural dynamics of the Herat fault, this work offers valuable insights into assessing the seismic hazard of the region, particularly for dense populations around Herat and Kabul.

Acknowledgments

References

Ambraseys, N., and R. Bilham (2003), Earthquakes in afghanistan, *Seismological Research Letters*, *74*(2), 107–123.

Boyd, O. S., C. S. Mueller, and K. S. Rukstales (2007), Preliminary earthquake hazard map of afghanistan, *US Geological Survey Open-File Report*, *2007*, 1137.

Dziewonski, A. M., T.-A. Chou, and J. H. Woodhouse (1981), Determination of earthquake source parameters from waveform data for studies of global and regional seismicity, *Journal of Geophysical Research: Solid Earth*, *86*(B4), 2825–2852.

Ekström, G., M. Nettles, and A. Dziewoński (2012), The global cmt project 2004–2010: Centroid-moment tensors for 13,017 earthquakes, *Physics of the Earth and Planetary Interiors*, *200*, 1–9.

Elliott, A., J. Elliott, J. Hollingsworth, G. Kulikova, B. Parsons, and R. Walker (2020), Satellite imaging of the 2015 m 7.2 earthquake in the central pamir, tajikistan, elucidates a sequence of shallow strike-slip ruptures of the sarez-karakul fault, *Geophysical Journal International*, *221*(3), 1696–1718.

Gisinger, C., L. Libert, P. Marinkovic, L. Krieger, Y. Larsen, A. Valentino, H. Breit, U. Balss, S. Suchandt, T. Nagler, et al. (2022), The extended timing annotation dataset for sentinel-1—product description and first evaluation results, *IEEE Transactions on Geoscience and Remote Sensing*, *60*, 1–22.

Hayes, G., G. Moore, D. Portner, M. Hearne, H. Flamme, M. Furtney, and G. Smoczyk (2018), Slab2, a comprehensive subduction zone geometry model, *Science*, *362*(6410), 58–61, doi:10.5066/F7PV6JNV.

Ischuk, A., R. Bendick, A. Rybin, P. Molnar, S. F. Khan, S. Kuzikov, S. Mohadjer, U. Saydullaev, Z. Ilyasova, G. Schelochkov, et al. (2013), Kinematics of the pamir and hindu kush regions from gps geodesy, *Journal of geophysical research: solid earth*, *118*(5), 2408–2416.

Kufner, S.-K., B. Schurr, C. Haberland, Y. Zhang, J. Saul, A. Ischuk, and I. Oimahmadov (2017), Zooming into the hindu kush slab break-off: A rare glimpse on the terminal stage of subduction, *Earth and Planetary Science Letters*, *461*, 127–140.

Lazeckỳ, M., K. Spaans, P. J. González, Y. Maghsoudi, Y. Morishita, F. Albino, J. Elliott, N. Greenall, E. Hatton, A. Hooper, et al. (2020), Licsar: An automatic insar tool for measuring and monitoring tectonic and volcanic activity, *Remote Sensing*, *12*(15), 2430.

Lazeckỳ, M., J. Fang, A. Hooper, and T. Wright (2022), Improved phase unwrapping algorithm based on standard methods, pp. 743–746, doi:10.1109/IGARSS46834.2022.9884337.

Lazeckỳ, M., Q. Ou, L. Shen, J. McGrath, J. Payne, P. Espín, A. Hooper, and T. Wright (2024), Strategies for improving and correcting unwrapped interferograms implemented in licsbas, *Procedia Computer Science*, *239*, 2408–2412.

Liu, Z., B. HAN, H. LIU, Z. LI, Y. NAI, B. CHEN, and J. PENG (2024), Seismogenic fault and building damage of the 2023 herat earthquake sequence revelated by radar interferometry, *Geomatics and Information Science of Wuhan University*, *49*(5), 722–733.

McNab, F., R. A. Sloan, and R. T. Walker (2019), Simultaneous orthogonal shortening in the afghan-tajik depression, *Geology*, *47*(9), 862–866.

Metzger, S., Ł. Gagała, L. Ratschbacher, M. Lazeckỳ, Y. Maghsoudi, and B. Schurr (2021), Tajik depression and greater pamir neotectonics from insar rate maps, *Journal of Geophysical Research: Solid Earth*, *126*(12), e2021JB022,775.

Morishita, Y., M. Lazecky, T. J. Wright, J. R. Weiss, J. R. Elliott, and A. Hooper (2020), Licsbas: An open-source insar time series analysis package integrated with the licsar automated sentinel-1 insar processor, *Remote Sensing*, *12*(3), 424.

Savage, J., and R. Burford (1973), Geodetic determination of relative plate motion in central california, *Journal of Geophysical Research*, *78*(5), 832–845.

Sborshchikov, I., L. Savostin, and L. Zonenshain (1981), Present plate tectonics between turkey and tibet, *Tectonophysics*, *79*(1-2), 45–73.

Shroder, J. F., N. Eqrar, H. Waizy, H. Ahmadi, and B. J. Weihs (2022), Review of the geology of afghanistan and its water resources, *International geology review*, *64*(7), 1009–1031.

Styron, R., and M. Pagani (2020), The gem global active faults database, *Earthquake Spectra*, *36*(1_suppl), 160–180.

Styron, R., M. Taylor, and K. Okoronkwo (2010), Database of active structures from the indo-asian collision, *Eos, Transactions American Geophysical Union*, *91*(20), 181–182.

Taylor, M., and A. Yin (2009), Active structures of the himalayan-tibetan orogen and their relationships to earthquake distribution, contemporary strain field, and cenozoic volcanism, *Geosphere*, *5*(3), 199–214.

Tian, D., L. Uieda, W. J. Leong, Y. Fröhlich, W. Schlitzer, M. Grund, M. Jones, L. Toney, J. Yao, Y. Magen, J.-H. Tong, K. Materna, A. Belem, T. Newton, A. Anant, M. Ziebarth, J. Quinn, and P. Wessel (2024), PyGMT: A Python interface for the Generic Mapping Tools, doi:10.5281/zenodo.13679420.

Watson, A. (2021), Interseismic practical, https://github.com/andwatson/interseismic_practical.

Watson, A. (2022), Decompose insar velocities, https://github.com/andwatson/decompose_insar_velocities.

Wessel, P., J. F. Luis, L. a. Uieda, R. Scharroo, F. Wobbe, W. H. Smith, and D. Tian (2019), The generic mapping tools version 6, *Geochemistry, Geophysics, Geosystems*, *20*(11), 5556–5564.

A Extra: Interactive PyGMT Visualizer

Generic Mapping Tools GMT is an open-source set of command-line tools widely used in the Earth sciences for generating publication-quality maps and illustrations (*Wessel et al.* (2019)). It generates maps by overlaying data in a layer-by-layer basis, storing resulting diagrams in PostScript format and typically exported as PDFs. A fully comprehensive interactive visualizer would therefore require a program that tracks every command used in creating the diagram to accurately gauge the position of a map relative to the background canvas. The significant manpower required to achieve this has been a major obstacle in developing the visualizer, despite this being a much-needed feature that would greatly enhance the user experience of GMT by streamlining workflows and also open the door for new interfaces to be developed.

More recently, GMT has been rebuilt as an Application Programming Interface (API) and can now be accessed in Python and associated interactive computing environments such as Jupyter Notebook via PyGMT (*Tian et al.* (2024)). Python's strength lies in its extensive ecosystem of libraries and versatile data visualization capabilities, which we take advantage of here to develop the first ever interactive GMT/PyGMT visualizer.

A.1 Code Development

The full interactive PyGMT visualizer library is available at github.com/chelle0425/IntPyGMT. This report was written with reference to version 1.0.0 of the library.

A.1.1 Borderless Mercator PNG

Our approach to the interactive visualizer originated from the simple idea of overlaying an interactive matplotlib map widget on top of a borderless PNG image. This is not limited to (py)GMT-generated outputs as it only depends on the coordinates of the lower-left and upper-right corners of the map. It is however limited to Mercator projection as conversion from clicks to map coordinates relies on matplotlib i.e. the overlaying matplotlib map must be perfectly aligned with the PNG image for coordinate retrieval to be accurate. The beauty of this functionality lies in its simplicity, allowing it to be extended to any PNG image, such as maps from papers where the original GMT code may not be available. Due to its versatility in both utility and integration with advanced functions, we chose to keep this as a separate function.
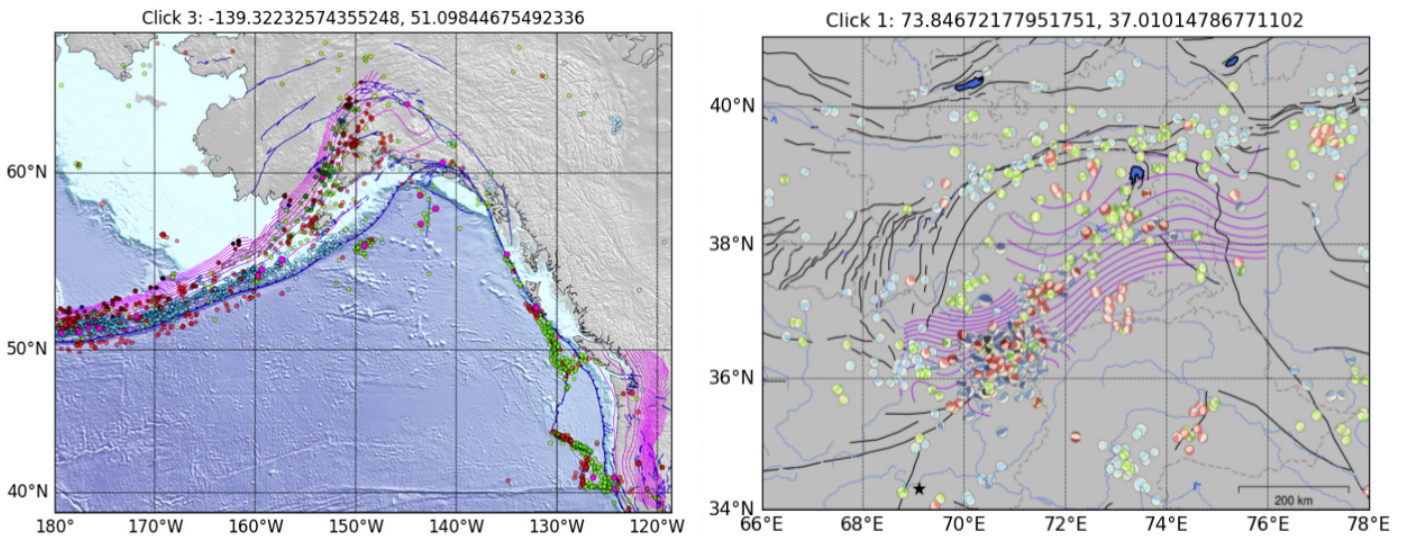

Figure 13: (Left) The original prototype interactive visualiser on Jupyter Notebook, hosted on GoogleColab and applied to a GMT-generated basemap. (Right) "Final" interactive visualiser available as a function within the IntPyGMT visualizer library, where much of the original code from the prototype remains. Notice the absence of (py)GMT-generated borders for the basemap — it took us the better part of the internship to find a workaround for this issue.

A.1.2 Interactive Time Series Viewer

After completing the base code, our first instinct was to apply it to an interactive time series viewer. The current COMET LiCSBAS tutorial materials used during the yearly international COMET InSAR Workshop is self-contained on Jupyter Notebook, with the exception of the final interactive time series, which is only available on Python (*Morishita et al.* (2020), used in Figure 5). An interactive time series viewer on Jupyter Notebook will allow the entire tutorial to be hosted on Jupyter Notebook, which when combined with web-based interfaces such as JupyterHub and Binder would greatly lower the barrier to entry for InSAR processing.

The advantage of a simple code that returns the longitude and latitude of a selected point is that we can easily feed its results into advanced functions for further data processing. Here, we do so by retrieving and plotting the time series data for the input coordinates, which is then saved and displayed alongside the interactive map.
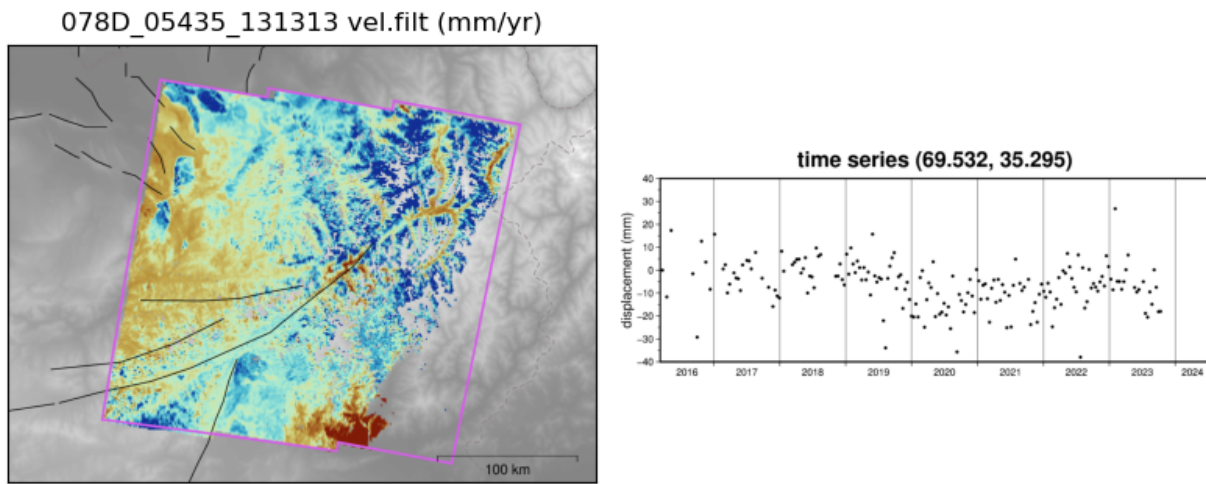

Figure 14: Interactive visualiser applied to descending frame 078D_05435_131313 and linked to a time series viewer function (right).

A.1.3 GMT/PyGMT-generated PNG

The initial library was quick to set up once the base functionality was in place. We then spent the next month extensively searching for how GMT determines the border width of a map relative to the background canvas. This was necessary if we wanted to extend the matplotlib map widget overlay across the entire canvas, allowing us to include map borders and legends. Despite our efforts however, it became clear that this information was not available anywhere online.

Instead of finding out how GMT calculates the border width of a map relative to the background canvas, we came up with the idea of manually specifying the border width (via xshift and yshift) on top of a blank canvas. Although this workaround has several limitations and requires more involvement when creating the initial (py)GMT map, it allowed us to extend this functionality to (nearly) any (py)GMT-generated PNG. We then integrated it with GMT's mapproject module to support any GMT-supported map projection, leveraging the fact that mapproject only requires the bottom-left corner coordinate of a map to determine coordinate conversions. Finally, we packaged everything into a python library, including demonstrations for both functions and detailed installation instructions.

B Appendices

B.1 LiCSBAS Processing Technicalities

The LiCSBAS processing workflow (Figure 15) illustrates the main processing steps involved in InSAR time series analysis for this study. With the exception of the singular approach at Step 1-3, the processing parameters used for both the initial frames and the final (merged) frame dataset were the same, and default settings were used unless otherwise specified. All parameter settings used in this study are listed in Appendix B.1.1 and B.1.3.
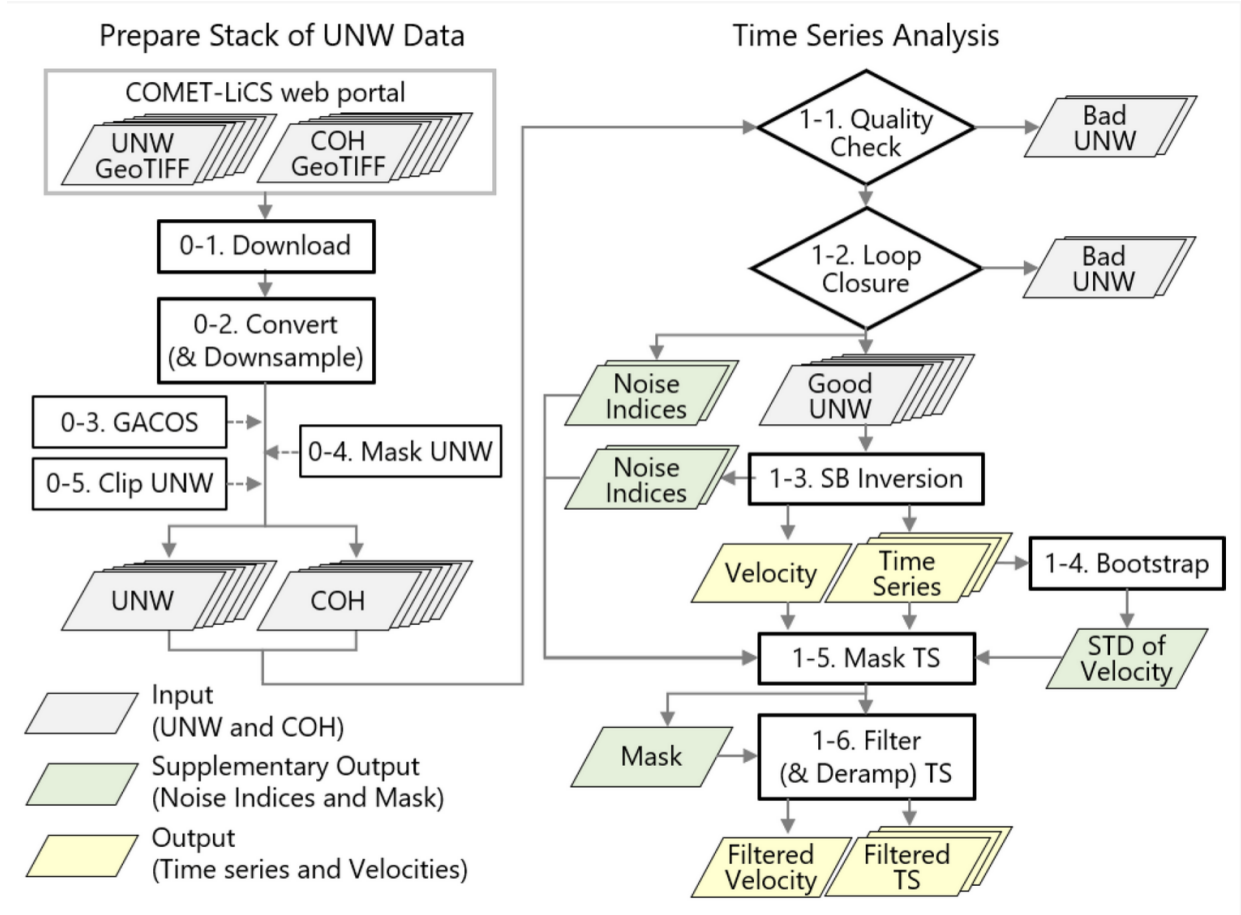

Figure 15: The LiCSBAS processing workflow involving five steps for data preparation (step 0–1 to 0–5) and six steps for time series analysis (step 1–1 to 1–6), after *Morishita et al.* (2020).

B.1.1 Initial Ascending and Descending Frames

The selected frames cover an observation period from March 9, 2016, to July 10, 2024. Additionally, we also employed the multi-prime mode in LiCSBAS Step 1-2, which accounts for bias during loop closure check. The processing parameters for the initial ascending frame 071A_05440_131313 are as follows:

LiCSBAS Step	Note
Step 1-1	
Step 1-2	-l 1.5 –nopngs –multi_prime –nullify
Step 1-3	–inv_alg WLS
Step 1-4	
Step 1-5	shown below
Step 1-6	–hgt_linear -r 1; see main article

And for descending frame 078D_05435_131313:

LiCSBAS Step	Note
Step 1-1	
Step 1-2	-l 15 –nopngs –multi_prime –nullify –ref_approx 168.7/36
Step 1-3	–inv_alg WLS
Step 1-4	
Step 1-5	shown below
Step 1-6	–hgt_linear -r 1; see main article

In addition to the above parameters, we applied tropospheric noise correction using GACOS at Step 0-3 and implemented reunwrapping using the licsar_extra repository (*Lazeckỳ et al.* (2022)) unless otherwise specified in text.

Figure 16 shows the masking parameters used at Step 1-5 for the ascending frame 071A_05440_131313, as seen in Figures 3, 2 & 5, and used in Figure 7.
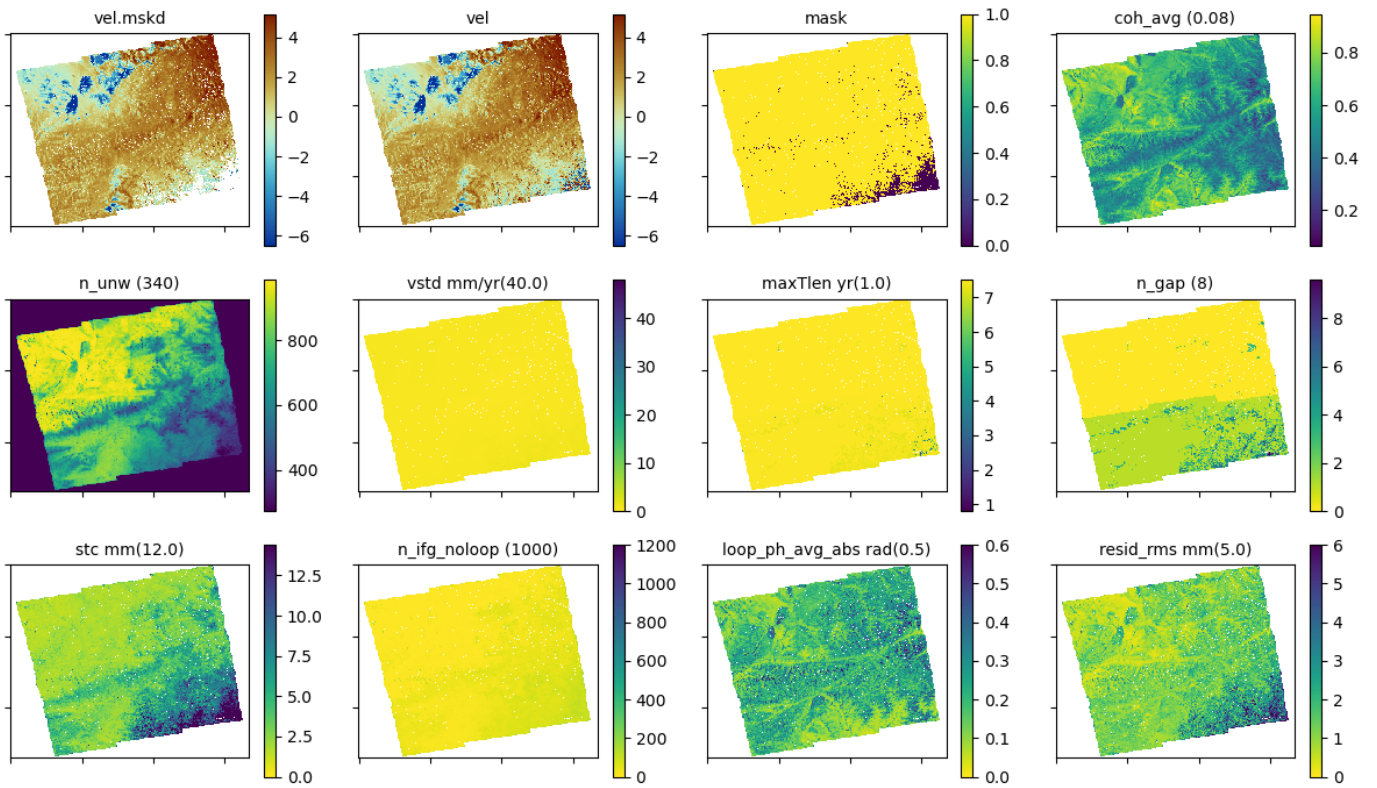

Figure 16: LiCSBAS Step 1-5 masking parameters for ascending frame 071A_05440_131313 (with reunwrapping applied). Note that we used the exact same masking parameters for both figures in Figure 3.

And the masking parameters for the descending frame 078D_05435_131313, as seen in Figure 2 and used in Figure 7.
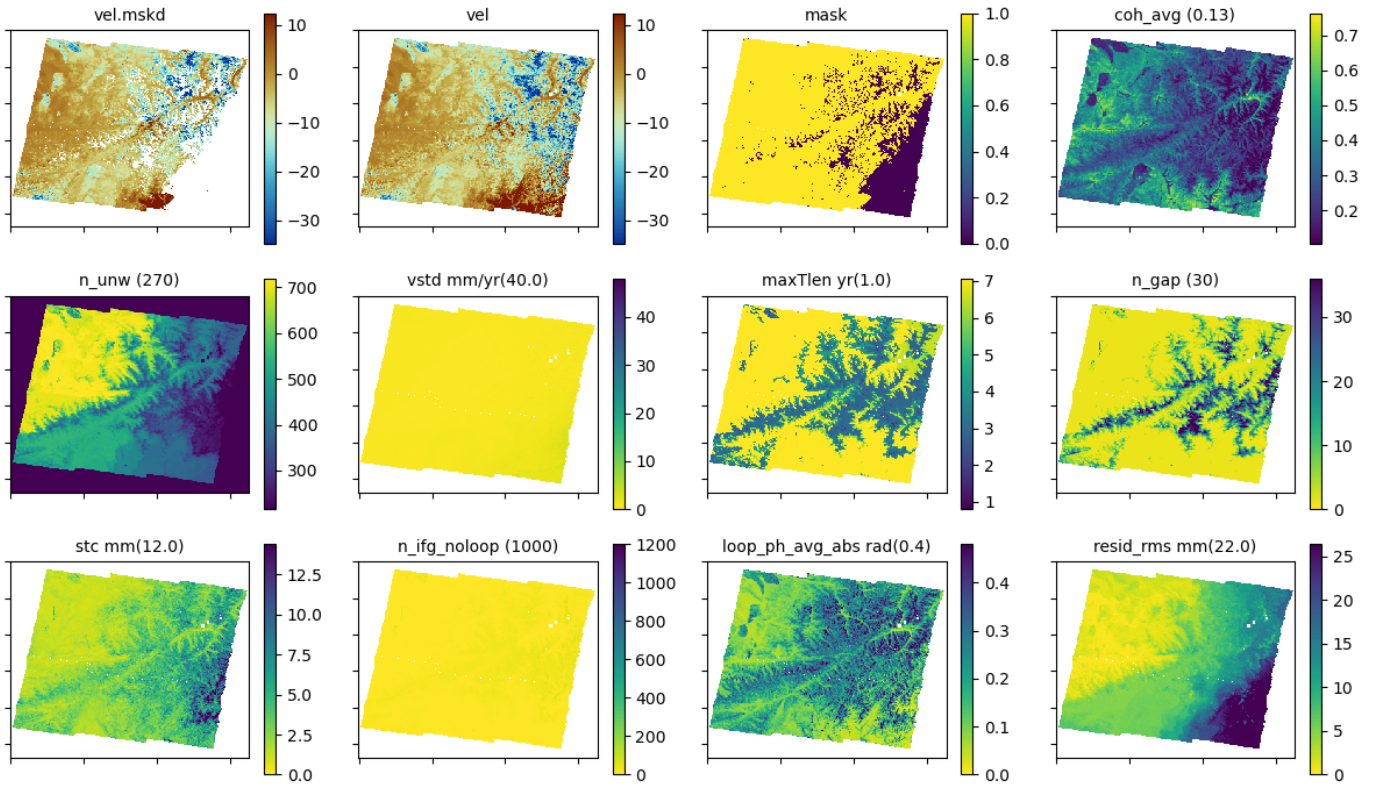
Figure 17: LiCSBAS Step 1-5 masking parameters for descending frame 078D_05435_131313 (with reunwrapping applied). Note that this does not apply to Figure 6, as no masking was applied.

B.1.2 LiCSBAS Step 1-3: Singular

We very soon realised that batch frame processing and merging for the Herat fault would be computationally expensive. The singular option available in Step 1-3 as an alternative to the standard NSBAS technique allows for a more computationally economic and faster solution. In theory, this is less accurate than NSBAS as it calculates the interpolating velocity used to link gaps in networks by adding the expected value to the last date before the gap, instead of determining the interpolating velocity via a full least squares inversion. A demonstration of the impact of this approach is shown in Figure 18.
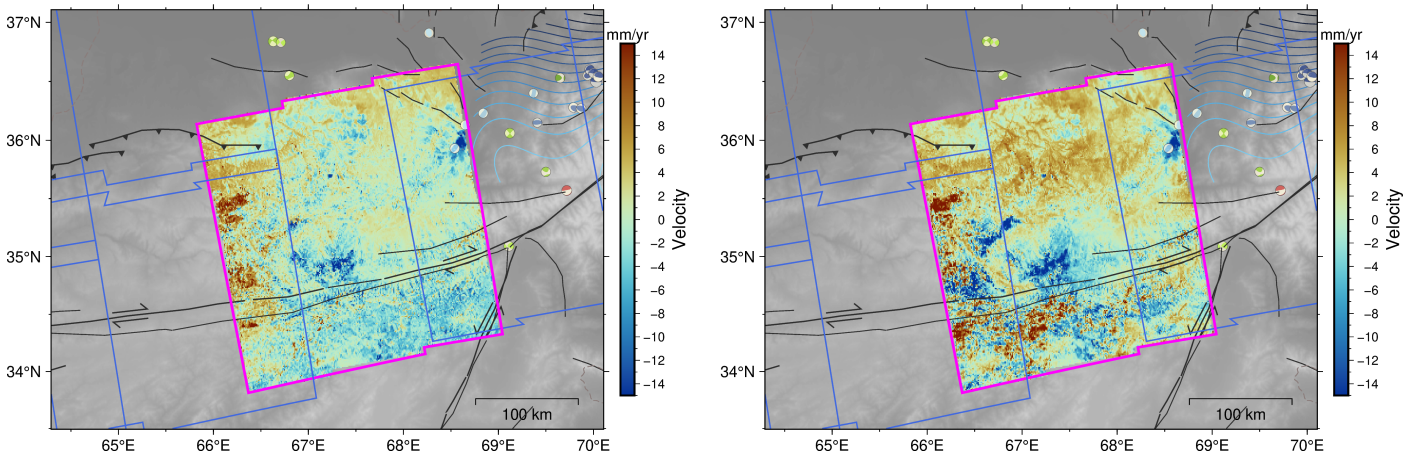

Figure 18: LiCSBAS Step 1-5 LOS velocity output (unmasked, without filtering) for ascending frame 144A_05476_141414, without (left) and with singular (right).

B.1.3   Final Merged Frames

Here are the full list of frame IDs for the final decomposed and merged velocities, selected to best cover the Herat fault. The selected frames cover an observation period from March 9, 2016, to October 1, 2023 (avoiding the 2023 Herat earthquake).

Final Merged Frame Pairs			
Ascending Pair		Descending Pair	
173A_05350_131313	Ascending	005D_05398_131313	Descending
042A_05535_131313	Ascending	049D_05534_131313	Descending
115A_05608_131313	Ascending	122D_05571_131313	Descending
115A_05409_131313	Ascending	122D_05372_131313	Descending
042A_05336_131313	Ascending	049D_05335_131313	Descending
071A_05440_131313	Ascending	078D_05435_131313	Descending
144A_05476_141414	Ascending	151D_05639_131313	Descending
144A_05476_141414	Ascending	151D_05440_131313	Descending

Table 1: Frame pairs for the final decomposed and merged velocities (Figure 9) Note the repeated use of ascending frame 144A_05476_141414 to ensure complete coverage of the Herat fault.

These frames were processed in batch on JASMIN and ARC4 using the following parameters (with default settings applied unless otherwise specified):

LiCSBAS Step	Note
Step 1-1	
Step 1-2	-l 1.5 –nopngs –multi_prime –nullify
Step 1-3	–inv_alg WLS –singular
Step 1-4	
Step 1-5	LiCSBAS default
Step 1-6	–hgt_linear -r 1

In addition to the above parameters, we also applied tropospheric noise correction using GACOS at Step 0-3 and implemented reunwrapping using the licsar_extra repository (*Lazeckỳ et al.* (2022)).

B.2 Appendix

Variable Analysis

The variables for the final merged frames were calculated as follows:

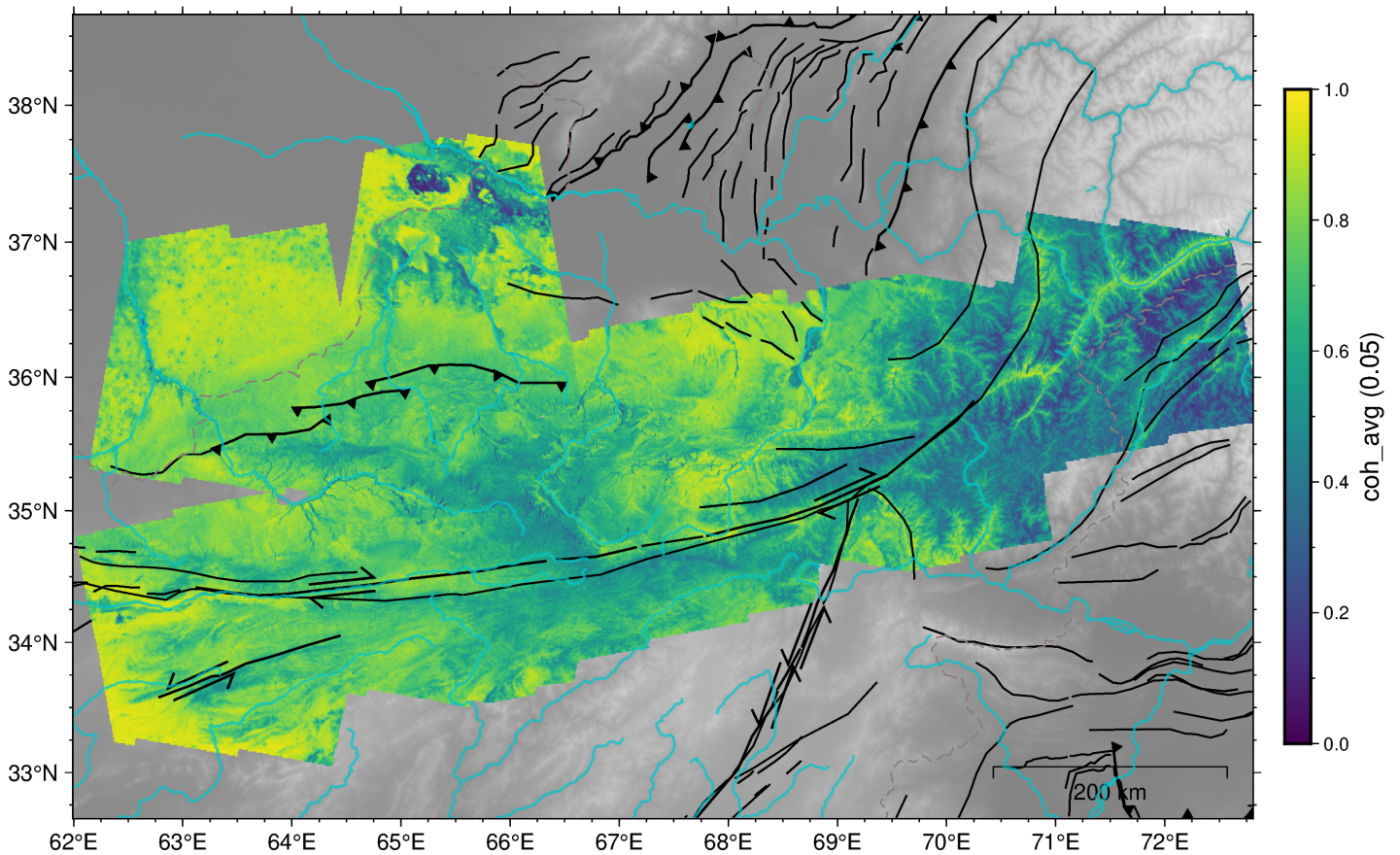| Noise Index	Variable	Derived from LOS frames by:
coh_avg	Average coherence	mean
loop_ph_avg_abs	Average loop phase closure error	mean
n_gap	Number of gaps	add
stc	Spatiotemporal consistency	add
resid_rms	Inversion residual RMS error	mean

Figure 19: Average coherence for the final decomposed and merged velocities (Figure 9), as the mean coherence of the ascending and descending frames. Note the low coherence observed in the Hindu Kush mountains to the east.

Harvard CMT Earthquake selection

Focal mechanism are from the Harvard Centroid Moment Tensor (CMT) Catalogue (*Dziewonski et al.* (1981), *Ekström et al.* (2012), globalcmt.org). We incorporated all events in the Hindu Kush region between the longitudes of 62°E to 84°E , and the latitudes 28°N to 45°N in the time interval between January 1, 1976, and July 10, 2024, unless otherwise specified.

B.3 Supplementary Material

All figures and codes used throughout this project are available at github.com/chelle0425/Leeds-Research-Internship.